Triple-phase ceramic 2D nanocomposite with enhanced thermoelectric properties[†]

Michael Bittner[1,*], Nikola Kanas[2], Richard Hinterding[1], Frank Steinbach[1], Dennis Groeneveld[1], Piotr Wemhoff[1], Kjell Wiik[2], Mari-Ann Einarsrud[2], Armin Feldhoff[1,*]

[1] *Institute of Physical Chemistry and Electrochemistry, Leibniz University Hannover, DE-30167, Hannover, Germany, Fax: +49(511)762-4009; Tel: +49(511)762-3555; E-mail: michael.bittner@pci.uni-hannover.de ; armin.feldhoff@pci.uni-hannover.de*

[2] *Department of Materials Science and Engineering, NTNU Norwegian University of Science and Technology, Sem Saelands vei 12, N-7491 Trondheim, Norway*

Abstract

A thermoelectric triple-phase p-type $Ca_3Co_4O_9$-Na_xCoO_2-$Bi_2Ca_2Co_2O_9$ (CCO-NCO-BCCO) 2D nanocomposite was obtained from pressureless sintering in air. The anisotropic thermoelectric properties of the nanocomposite exhibit a high electrical conductivity of 116 $S \cdot cm^{-1}$ and a power factor of 6.5 $\mu W \cdot cm^{-1} \cdot K^{-2}$ perpendicular to the pressing direction at 1073 K in air. A corresponding zT value of 0.35 was obtained. Three co-doped, thermoelectrically active misfit-layered materials were stacked to form a triple-phase nanocomposite, which combines the advantages of all three materials. The resulting nanocomposite enables simultaneous increases of the isothermal electrical conductivity σ and the Seebeck coefficient α by charge carrier concentration engineering and synergistic effects. The $Bi_2Ca_2Co_2O_9$ and Na_xCoO_2 phases were stabilized in a $Ca_3Co_4O_9$ matrix at high temperatures. To evaluate the application of the nanocomposite in high-temperature thermoelectric generators, the representation of the electrical conductivity and power factor in a Ioffe plot was more appropriate than the zT value.

[†] Electronic Supplementary Information (ESI) available.

Keywords: Thermoelectricity; All-scale hierarchical architecture; 2D nanostructures; Nanocomposite; $Ca_3Co_4O_9$

1. Introduction

1.1. Thermoelectric power conversion

Interest in thermoelectric materials (TE) for energy harvesting arises from their ability to convert thermal power directly into electrical power without moving parts. This is mediated by the coupling of currents of entropy I_S and electrical charge I_q in the solid, which can cause a thermally-induced electrical current (Seebeck effect). Under steady state conditions and the assumption of weak temperature dependence of the electron chemical potential as well as of the Seebeck coefficient α, the basic transport equation [1, 2] can be expressed by the difference in temperature ΔT and the electrical voltage U over the thermoelectric material of cross-sectional area A and length L as follows:

$$\begin{pmatrix} I_q \\ I_S \end{pmatrix} = \frac{A}{L} \cdot \begin{pmatrix} \sigma & \sigma \cdot \alpha \\ \sigma \cdot \alpha & \sigma \cdot \alpha^2 + \Lambda \end{pmatrix} \cdot \begin{pmatrix} U \\ \Delta T \end{pmatrix} \quad (1)$$

The thermoelectric material tensor in Equation 1 is composed of three quantities, which are the isothermal electrical conductivity σ, the Seebeck coefficient α and the entropy conductivity at electrical open circuit Λ (i.e., at vanishing electrical current). Note that each quantity σ, α and Λ itself is a tensor. The entropy conductivity Λ is related to the traditional heat conductivity λ by the absolute temperature T, as given in Equation 2.

$$\lambda = T \cdot \Lambda \quad (2)$$

The maximum of the second-law power conversion efficiency $\eta_{II,max}$ is determined solely by the thermoelectric figure-of-merit zT, as given by Equation 3, which results from tensor element 22 in the thermoelectric material tensor in Equation 1 [1].

$$zT = \frac{\sigma \cdot \alpha^2}{\Lambda} = \frac{\sigma \cdot \alpha^2}{\lambda} \cdot T \quad (3)$$

Maximum electrical power output of a thermoelectric material $P_{el,max,mat}$, as shown in Equation 4, is deter-

mined by the geometry (A, L), the power factor $\sigma \cdot \alpha^2$ and the temperature difference to the square $(\Delta T)^2$.

$$P_{el,max,mat} = \frac{1}{4} \cdot \frac{A}{L} \cdot \sigma\alpha^2 \cdot (\Delta T)^2 \quad (4)$$

The laws of classical physics restrict the scope for enhancing the power factor $\sigma \cdot \alpha^2$ and figure-of-merit zT due to the interrelation of the parameters σ, α and λ. These values depend on the carrier concentration n and the mobility of the carriers μ, which correlate with each other [3].

To overcome these limits, several approaches have been postulated and tested during recent years. Previously, the thermoelectric community was focused on reducing λ and thereby optimizing zT. This was performed by tuning the micro- and nanostructure to scatter phonons on all length scales [7, 8]. The best material would possess an all-scale hierarchical architecture that scatters phonons on the mesoscale by it's microstructure, on the nanoscale by nanoprecipitates or nanostructures and on the atomic scale by point defects (co-doping, cross substitution) [9, 10]. The structures should be coherent (endotaxy) and possess electronic band energies matching those of the host material to avoid electron scattering, which would result in reduced electron mobility [11, 12, 13].
Recently, more attention has been paid to enhancing the power factor $\sigma \cdot \alpha^2$ [14, 15, 16, 17]. Carrier concentration engineering and co-doping can be used to increase the electrical conductivity σ [10]. The approaches of compositionally alloyed nanostructures and band-structure engineering are able to increase the Seebeck coefficient α [11, 13]. The most promising approach to enhance the power factor in an almost temperature-independent manner is band-structure engineering with resonant levels or resonant impurities and the introduction of additional electronic bands [14, 18]. The goals of this effort are the distortion and increase of the electronic density of states (DOS) in the vicinity of the Fermi level as much as possible. Hicks and Dresselhaus forecasted nanostructures such as 2-dimensional (2D) quantum wells and 1D quantum wires to be suitable for tuning the DOS in the vicinity of the Fermi level by the aforementioned techniques [19].

1.2. Oxides

State-of-the-art commercially available bulk thermoelectric materials include alloys, tellurides and half-Heusler or Zintl phases, such as Bi_2Te_3 [20], PbTe-PbS [16], SiGe [21], SnSe [22], FeNbSb [17] and $Yb_{14}MnSb_{11}$ [23]. These materials exhibit inferior stability at high temperature and in oxidizing atmospheres, are toxic, or include expensive and rare elements. However, thermoelectric oxides are expected to be viable materials for addressing these problems due to their benefits, such as non-toxicity, mechanical, thermal and chemical stability at high temperatures in air [24, 25, 26].
Recently, a new thermoelectric oxide material was discovered: BiCuSeO oxyselenides possess excellent thermoelectric properties in the moderate-temperature range (up to 650 °C), being comparable to alloys, Half-Heusler and Zintl phase materials [27, 28, 29]. However, BiCuSeO oxyselenides are not stable at high temperatures under oxidizing conditions [30]. In terms of the figure-of-merit zT, oxides which are stable in air can not compete with other material classes. For this reason, the development of oxides should focus on high power factors and electrical conductivity, to enhance the electrical power output of thermoelectric generators at high temperatures. Narducci postulated that if an infinite heat source is available for thermoelectric energy conversion, a high power factor and a moderate heat conductivity are beneficial for high electrical power outputs [31].
The layer-structured cobalt oxide $Ca_3Co_4O_9$ (CCO), based on CaO, has already been investigated and sustains high temperatures up to 1198 K [32, 33, 34]. CCO possesses a monoclinic crystal structure formed by a misfit-layered structure of a CdI_2-type CoO_2 subsystem with a triangular lattice and a layered rock-salt subsystem of three Ca_2CoO_3 units, which alternate along the c-axis. The two subsystems of the monoclinic system have different b-axis parameters and form an incommensurate structure, as shown in Figure 1a [4]. The synthesis of doped CCO via the well known sol-gel technique, reveals several advantages such as homogeneity, grain size and stoichiometric control [33]. The layered crystal structure affects also grain shape and has significant impact on anisotropy, degree of compacting and thereby on thermoelectric properties, especially on isothermal electrical conductivity and heat conductivity. In this work, sol-gel synthesis is used as a "bottom-up" technique to co-dope Na, Bi and Tb to the Ca-site of the Ca_2CoO_3 subsystem, which is visualized in Figure 1a. Table S 1† in the supplementary information shows the ionic radii of the substituted elements and dopants. According to the similarity of the ionic radii, doping should be possible. Co-doping can adjust carrier concentrations and introduce resonant impurities to enhance the thermoelectric properties σ and α. According to Equation 4, this directly improves the electrical power outputs of the obtained materials. Thus, σ can

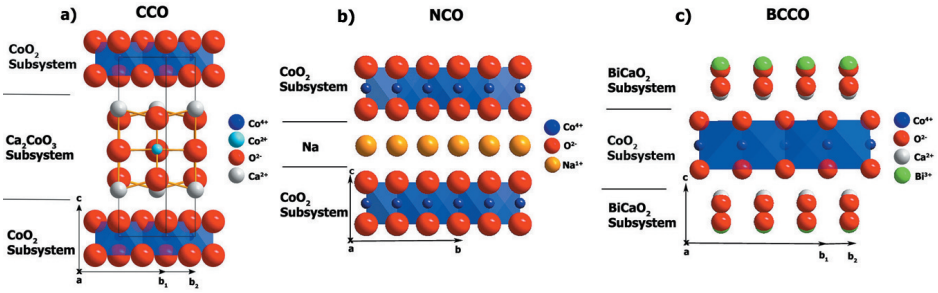

Figure 1: Crystal structures of a) $Ca_3Co_4O_9$ (**CCO**), b) Na_xCoO_2 (**NCO**) and c) $Bi_2Ca_2Co_2O_9$ (**BCCO**) along the *a*-axis. The ions involved are indicated by spheres of different size and colour: cobalt (small) in blue and turquoise, oxygen (large) in red, calcium (medium) in grey, bismuth (large) in green and sodium (large) in orange. Note b_1 and b_2 in a), b) form an irrational ratio, and the aperiodic crystal structure is described by superspace groups. Crystal structure data were taken from [4, 5, 6].

be enhanced by Na and Bi doping [10, 35, 36], while α can be improved by rare-earth doping (Tb) due to the hybridization of electronic bands with *sp* character [13, 26, 37, 38].

Increasing the doping level of Na and Bi leads to the formation of a triple-phase nanocomposite of co-doped CCO, Na_xCoO_2 (NCO) and $Bi_2Ca_2Co_2O_9$ (BCCO). NCO and BCCO also have monoclinic misfit-layered crystal structures, revealed in Figure 1b,c, which are comparable to that of CCO [4, 6, 39, 40]. The three structures simply differ in stacking and composition of the rock salt layer. Compared to CCO, BCCO possesses a higher α but a lower σ and NCO vice versa [6, 41, 42]. Overall, a nanocomposite (CCO-NCO-BCCO) of a co-doped CCO phase and "compositionally alloyed nanostructures" [10] of NCO and BCCO with partially coherent layered structures promise enhanced thermoelectric properties compared to those of the single materials. The formation of a high power triple-phase nanocomposite stabilizes the NCO and BCCO phases at elevated temperatures and hence enables application in thermoelectric generators for energy conversion.

2. Materials and Methods

2.1. Synthesis

Different elements like Li, Ce, Sm and Yb next to Na, Bi and Tb were tested as dopants for CCO. The best combination was found to be Na, Bi and Tb. Na, Bi and Tb co-doped CCO powders were synthesized via a sol-gel route, which provides fine-grained particles of homogenous composition as described by [43] for perovskites and by [33] for pure CCO. Calcium(II) nitrate tetrahydrate 99.98 %, cobalt(II) nitrate hexahydrate ACS 98-102.00 %, bismuth(III) nitrate hydrate 99.999 %, terbium(III) nitrate hydrate 99.9 % and sodium nitrate ≥ 99.5 % from Alfa Aesar were used as sources. The calcined powder samples were uniaxially cold pressed at 200 MPa and pressurelessly sintered in air for 20 h at 1173 K. Reference samples of CCO, BCCO and NCO phases were cold pressed at 200 MPa and sintered for 10 h at 1173, 1123 and 1073 K, respectively. Table 1 shows the stoichiometry and abbreviation of synthesized samples. All steps, synthesis, calcination and sintering, were conducted under ambient air conditions.

Table 1: Stoichiometry and abbreviation of synthesized nanocomposites (CCO-30-35-6, CCO-30-35-8, CCO-30-35-10) and reference samples (CCO, BCCO, NCO).

stoichiometry	abbreviation
$Ca_3Co_4O_9$	**CCO**
Na_xCoO_2	**NCO**
$Bi_2Ca_2Co_2O_9$	**BCCO**
$Ca_{2.29}Na_{0.3}Bi_{0.35}Tb_{0.06}Co_4O_9$	**CCO-30-35-6**
$Ca_{2.27}Na_{0.3}Bi_{0.35}Tb_{0.08}Co_4O_9$	**CCO-30-35-8**
$Ca_{2.25}Na_{0.3}Bi_{0.35}Tb_{0.1}Co_4O_9$	**CCO-30-35-10**

2.2. Microstructure analysis

The phase compositions of the synthesized powders and sintered ceramics were characterized via X-ray diffraction (XRD) using a Bruker D8 Advance with Cu-K_α radiation. Microstructural characterization and elemental analysis of polished ceramic samples were performed using a JEOL JSM-6700F field-emission scanning electron microscope (FE-SEM) equipped with an Oxford Instruments INCA 300 (energy-dispersive X-ray spectroscopy, EDXS). Transmission electron microscopy (TEM) was performed at 200 kV using a JEOL

JEM-2100F-UHR equipped with an Oxford Instruments INCA 300 (EDXS) for elemental analysis. Elemental distribution information of analyzed materials were obtained from Na-K_α, Ca-K_α, Bi-L_α, Co-K_α, Tb-L_α and O-K_α transitions. Density and porosity were measured by Archimedes method (ISO 5018:1983) using isopropanol. Density values were averaged from 3 measurements with less than 2 % deviation. The heat capacity C_P, was estimated by differential scanning calorimetry (DSC) with a Netzsch STA 409 PC/PG in a synthetic air atmosphere with a flow of 30 mL $\cdot$ min^{-1} and a heating rate of 5 K $\cdot$ min^{-1} within the range of 313 K to 1173 K.

2.3. *Measurement of thermoelectric properties*

To investigate the thermoelectric properties of the manufactured oxide materials, σ, α and λ were measured as functions of temperature and pressing direction. To obtain a large ceramic sample (CCO-30-35-6, 30-35-8 and 30-35-10), the green body was pressed at 200 MPa using a 16 mm die and reground and pressed again, followed by a sintering process of 20 h at 1173 K. Samples were cut from large ceramic pellets (cylindrical, 16 mm $\cdot$ 16 mm) in bar shape (10 mm $\cdot$ 1.2 mm $\cdot$ 1.2 mm and 10 mm $\cdot$ 2.5 mm $\cdot$ 2.5 mm) parallel and perpendicular to the pressing direction. The σ values were estimated by a pseudo 4-point measurement at equilibrium conditions, utilizing a horizontal three-heating-zone tube furnace from Carbolite Gero EVZ 12/450B and a home-made measurement cell. The α values were measured using a ProboStat A setup from NorECs at equilibrium conditions in a furnace from Elite Thermal Systems Ltd. The values were logged using KEITHLEY 2100 $6\frac{1}{2}$ Digital Multimeters. Data were acquired and converted using Lab VIEW software. The measurements of σ and α (heated to 1073 K and measured down with equilibrium at every temperature) were repeated from samples cut perpendicular and parallel to the pressing direction with less than 5 % deviation. The uncertainties of 5 and 2 % for α and of 10 and 4 % for the power factor (the latter obtained from samples cut parallel to the pressing direction), were averaged from 5 values. The values of λ were estimated using $\lambda = D \cdot C_P \cdot \rho$ and a LFA 457 MicroFlash laser flash setup from Netzsch under synthetic air atmosphere. Measurements of the thermal diffusivity D, averaged from 3 values, showed less than 5 % deviation. Accordingly, the uncertainties for the zT value were calculated to be 10 and 5 % (the latter obtained from samples cut parallel to the pressing direction). More details are given in the supporting information[†].

3. Results and Discussion

3.1. *Composition of triple-phase nanocomposites*

The XRD patterns of all three phases (CCO, NCO, BCCO) within the triple-phase nanocomposite are shown as individual references in Figure 2a-c. With increasing doping level above the solubility limit of the CCO matrix, the formation of a composite material consisting of CCO, NCO and BCCO phases during sintering at 1173 K was enabled, as shown in Figure 2d-g.

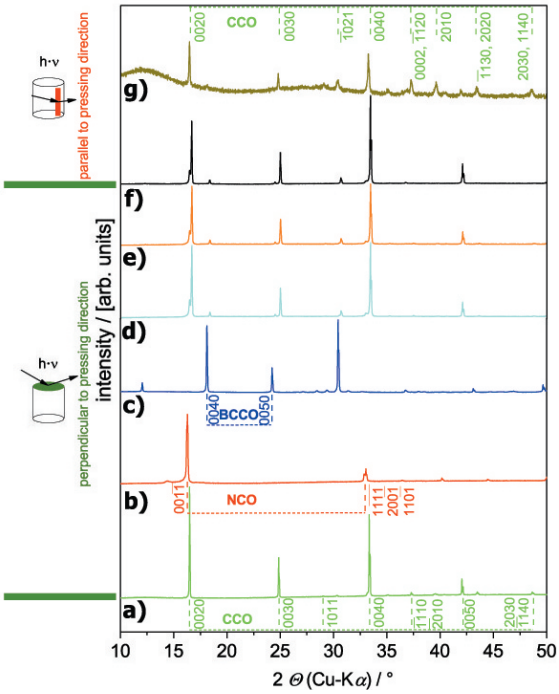

Figure 2: X-ray diffraction patterns of ceramic samples: a) **CCO** (taken from [33]), b) **NCO**, c) **BCCO**, d) **CCO-30-35-6**, e) **CCO-30-35-8**, f) **CCO-30-35-10** (perpendicular to pressing direction), g) **CCO-30-35-10** (parallel to pressing direction). CCO (green) and BCCO (blue) reflections were indexed in superspace group Cm (0 1 - p 0, equivalent to Bm (0 0 γ), no. 8.3 [44, 40]). NCO (red) reflections were indexed in superspace group C2/m [6]. The main NCO reflections (001-1 and 22-1-1, 200-1, 110-1) overlap with CCO (green) reflections. Difference in texture was obtained from samples, which were cut perpendicular (d-f) and parallel to the pressing direction (g). Additional XRD patterns of NCO and BCCO are given in S1[†].

As the Tb content was increased, the ceramics became slightly more textured and oriented compared with the CCO reference in Figure 2a (weaker 0020,

Table 2: Density and porosity of reference ceramics (CCO, NCO, BCCO) and nanocomposite ceramics. References were sintered for 10 h at 1173, 1123, 1073 K and nanocomposites for 20 h at 1173 K. Values of the density were measured using ISO (International Organization for Standardization) 5018:1983. Reference values for CCO are taken from [33]. True density of composite ceramics is unknown.

material abbreviation	bulk density / g $\cdot cm^{-3}$	true density / g $\cdot cm^{-3}$	open porosity / %	true porosity / %	closed porosity / %	theoretical density / %
CCO	3.2 ± 0.1	4.68	33.3 ± 0.7	33.5 ± 1.1	0.2 ± 0.7	67.7 ± 1.5
NCO	3.2 ± 0.0	4.65	15.7 ± 2.6	30.6 ± 0.2	14.9 ± 2.8	69.4 ± 0.0
BCCO	5.5 ± 0.0	6.82	1.6 ± 0.9	19.8 ± 0.6	18.1 ± 0.4	80.2 ± 0.0
CCO-30-35-6	3.9 ± 0.0		21.5 ± 0.3			
CCO-30-35-8	3.9 ± 0.0		22.1 ± 0.9			
CCO-30-35-10	3.9 ± 0.0		19.2 ± 0.7			

2010 and stronger 0040, 0050 CCO reflections). Furthermore, the reflections were less shifted to lower angles with increasing Tb-content. Hence, Tb was assumed to facilitate the formation of the CCO-NCO-BCCO nanocomposite, and smaller amounts of Bi were integrated into the CCO structure. Reflections of the NCO (001-1) and BCCO (0040, 0050) phases can be found within the nanocomposites, as shown in Figure 2d-g. Depending on the direction of cold pressing and cutting of the ceramic green body, different texture was obtained, as displayed in Figure 2d-f (perpendicular) and Figure 2g (parallel). Parallel to the direction of cold pressing of the green body, the ceramic showed a more variegated mixture of reflections from different planes, although the reflections 00*l*0 (0020, 0030, 0040, etc.) remained the most intense.

Supplementing the XRD patterns, microstructural characterization by SEM revealed the NCO phase and confirmed the CCO and BCCO phases within the composite material. The microstructure of NCO and BCCO phases are displayed in Figure S 2[†], while SEM micrographs and elemental distributions of polished cross-sections of CCO-NCO-BCCO nanocomposites are shown in Figure 3. The representation of the elemental Tb content in the SEM mappings was resigned due to the homogenous distribution on the microscale and therefore missing scientific information. Values of the density of NCO and BCCO are given in Table 2. Co-doping with Na, Bi and Tb resulted in a nanocomposite material of CCO, BCCO and NCO grains with pores in between. Increasing the doping level of Tb led to the formation of a denser nanocomposite, as shown in Figure 3a-f, and subsequently decreased porosity, given in Table 2. This porosity has a strong impact on thermal and electrical conductivity, because both values are decreasing with increased thermal and electrical contact resistances [33, 34]. The values of both, thermal and electrical conductivity, are also influenced by the degree of grain orientation, since the grains have anisotropic transport characteristics. Moreover, the higher the grain orientation, the lower is the porosity.

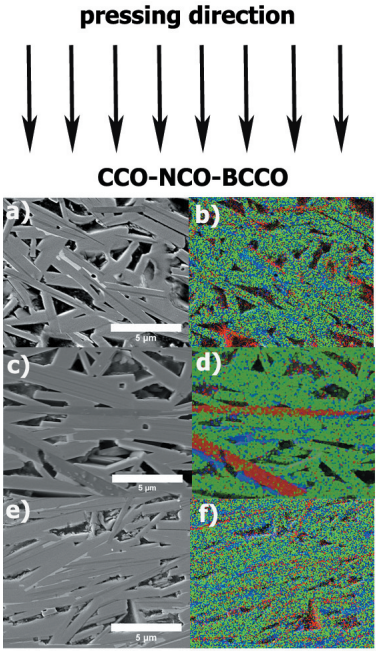

Figure 3: Cross-sectional SEM micrographs and EDXS elemental distributions of CCO-NCO-BCCO nanocomposite ceramics: a, b) **CCO-30-35-6**; c, d) **CCO-30-35-8**; e, f) **CCO-30-35-10**. The CCO phase is dominated by Ca (green), the NCO phase by Na (red) and the BCCO phase by Bi (blue). The direction of uniaxial cold pressing is indicated by black arrows. Additional SEM sites of NCO and BCCO are shown in Figure S 2[†].

The CCO-30-35-10 nanocomposite was further examined by TEM. Figure 4a-f identifies semi-coherently aligned 2D nanostructures. The material was pervaded by NCO, BCCO and CCO 2D layers, revealed in Figure 4a,b. These layers were homogeneously distributed throughout the material, alternating in thickness and sequence. As shown in Figure 4b,c, the different layers were co-doped with Na, Bi and Tb in the CCO phase,

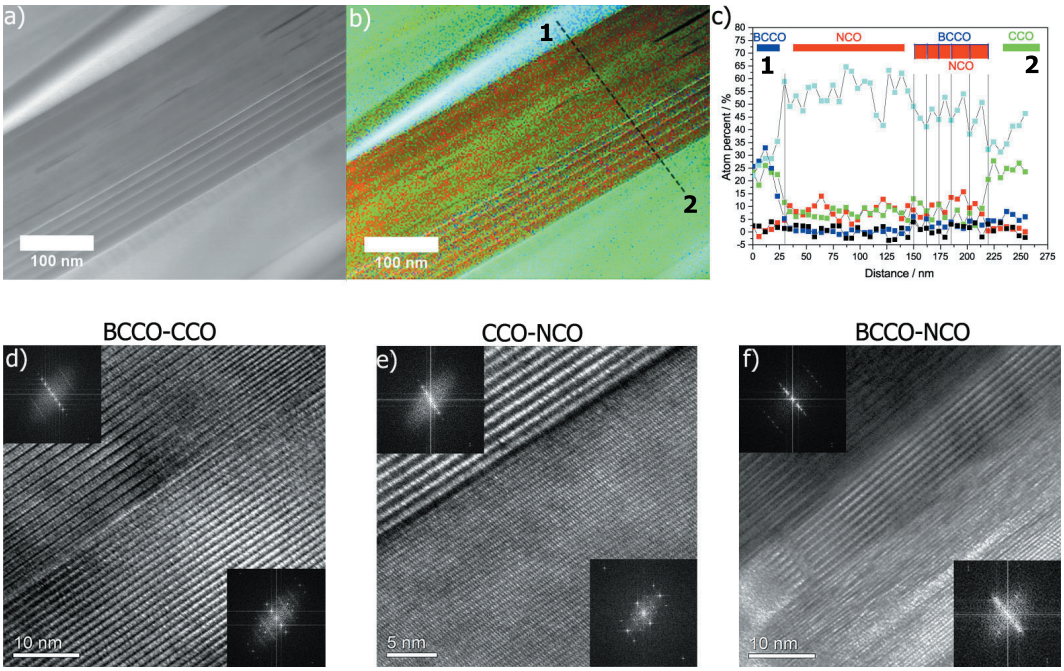

Figure 4: TEM analysis of a **CCO-30-35-10** nanocomposite ceramic: a, b) Scanning transmission electron microscopy (STEM) dark-field micrograph and EDXS elemental distribution (more detail in Figures S 3, 4†). The CCO phase is dominated by Ca, the NCO phase by Na and the BCCO phase by Bi. c) Linescan of 5.7 nm point-to-point distance of the elemental distribution of Na (red), Ca (green), Bi (blue), Tb (black) and Co (turquoise) in the area shown in b) and along the indicated dotted line. d-f) High-resolution transmission electron microscopy (HRTEM) micrographs of the heteromaterial interfaces BCCO-CCO, CCO-NCO and BCCO-NCO. Insets show the reduced fast Fourier transformation (rFFT), which are shown in more detail in Figure S 5†. Additional TEM sites are shown in Figures S 6-8†.

Ca, Bi and Tb in the NCO phase, and Na and Tb in the BCCO phase, respectively. The Tb content was enriched in the CCO and BCCO, while decreased in the NCO phase.

Table 3: Lattice parameters (in Å) of the CCO, NCO and BCCO phases at the interfaces BCCO-CCO, BCCO-NCO and CCO-NCO within a CCO-30-35-10 nanocomposite, as analyzed by HRTEM (Figure 4). Values were measured from reduced fast Fourier transformations (rFFT). Semi-coherent lattice parameters are in bold.

	Interfaces		
	1) BCCO-CCO	3) BCCO-NCO	2) CCO-NCO
BCCO	c=15.02	b_1=3.13, c=14.81	
CCO	**a=5.11**, b_2=4.55 c=10.96		c=10.67
NCO		**a=5.26**, c=5.47	**a=5.07**, b_1=2.82 c=5.74

These co-doped layers of NCO and BCCO seemed to be stabilized at high temperatures by the interdiffusion of the doped elements and surrounding phases, represented in the linescan of Figure 4c. The NCO phase, not implemented in the nanocomposite, exhibited the lowest chemical and thermal stability at high temperatures. As illustrated in Figure 5a, the NCO reference phase began decomposing in air at approximately 963 K. Although, the interdiffusion of Ca, Bi and Tb, as shown in Figure 4c, could stabilize this phase (Bi and Tb may occupy Na positions). The effect of the interdiffusion of Ca into the NCO phase also seemed to depend on the its thickness and surroundings. Figure 4d-f reveals the three feasible heterophase interfaces, BCCO-CCO, CCO-NCO and BCCO-NCO within the nanocomposite. The different phases grew semi-coherently on each other, facilitated by their similar, layered structure. The lattice parameters, given in Table 3, show similar values for the *a*-axis, while the *c*-parameter within the different phases was slightly lower than a multiple of the *c*-parameter in NCO. The NCO phase also exhibited areas of amorphous-like character with many defects, as displayed in Figure 4f. This phase was naturally less stable, but the amorphous-like phase formation could be either attributed to very thin layers, a cation-deficient metastable phase or damage from Ar-ion polishing dur-

ing specimen preparation. Analyzes from SEM and TEM, as shown in Figures 3 and 4, revealed structures on the micro- and nanoscale. Figure 4c confirmed point defects on the atomic scale, which were introduced by interdiffusion and co-doping. Overall, structural investigations verified an all-scale hierarchical structure of the nanocomposites. Hence, phonons could be scattered on the microscale, nanoscale and atomic scale, while at the same time, semi-coherently aligned, misfit-layered materials were present as shown.

3.2. Thermoelectric properties

The thermoelectric properties of reference NCO and BCCO materials are shown in Figure 5. The NCO material shows a high electrical conductivity of 142 S · cm^{-1} at 963 K, but low Seebeck coefficient of 175 μV · K^{-1} at 873 K. The NCO material decomposes at about 963 K in air, leading to a decreased conductivity. In contrast to this, the BCCO material has a high Seebeck coefficient of 274 μV · K^{-1} at 973 K, but a low electrical conductivity of 18 S · cm^{-1} at 1023 K. The BCCO material is stable up to 1023 K in air.

The thermoelectric properties of CCO and nanocomposites are based on an anisotropic character, as shown in Figure 6. This anisotropy is caused by the crystal structures of the three basic materials CCO, NCO and BCCO, as illustrated in Figure 1a-c, and by compression and sintering, which led to grain orientation, as shown in Figures 2, 3 and 4. The thermoelectric properties σ, α and power factor of CCO and the nanocomposite ceramics, are illustrated in Figure 6a,b as a function of temperature and depend on the pressing direction. The trend for σ for all samples, displayed in Figure 6b, was almost constant throughout the temperature range and reached 116 S · cm^{-1} at 1073 K for CCO-30-35-10 perpendicular to the pressing direction. The σ values of CCO and of CCO-30-35-10 were also measured parallel to the pressing direction and reached 48 S · cm^{-1} and 51 S · cm^{-1}, respectively, at 1073 K. These materials showed similar behavior because of the enhanced orientation and nanocomposite composition in CCO-30-35-10. As shown in Figure 3, the nanocomposite ceramics contained not only a Na, Bi and Tb co-doped CCO phase, but also NCO phase [6, 45], which is electrically highly conductive, as indicated in Figure 5a. It is concluded, that the incorporated and stabilized, co-doped NCO phase further increased the σ value of the nanocomposite material. Both, the formation of a BCCO phase, which has a high α value [41, 42], as illustrated in Figure 5b, and the integration of Bi and Tb [38] at Ca-site positions, increased the α value of the nanocomposite. The NCO and BCCO materials show

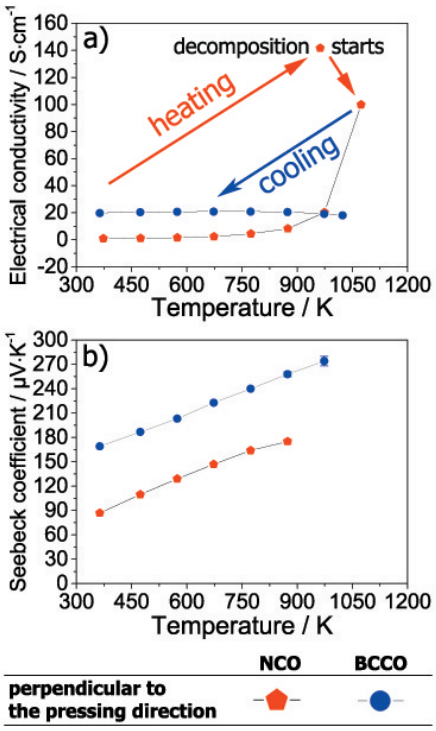

Figure 5: Thermoelectric parameters of **NCO** (pentagon, red) and **BCCO** (circle, blue) as a function of temperature in air: a) Isothermal electrical conductivity σ, direction of heating, cooling, start of NCO decomposition and highest value of NCO before decomposition are indicated. b) Seebeck coefficient α. Samples were cut and measured perpendicular to the pressing direction. Uncertainties are indicated by error bars.

inferior stability at temperatures above 963 and 1023 K in air, respectively, as shown in Figure 5. However, the incorporation of NCO and BCCO into a stable matrix like CCO stabilized these materials at high temperatures (above 963 K, 1023 K) in air. As long as nanocomposites are used up to 1073 K, they show good cycle stability. A different manuscript, which addresses stability and thermoelectric generators is going to be published soon. The generators were annealed at least two times up to 1073 K and subsequently tested from 973 to 1173 K in air. The results were stable and in accordance with the thermoelectric properties of the single materials. For this reason, the microstructure of the nanocomposites is assumed to be stable and unchanged. The behavior of α for all nanocomposites, shown in Figure 6a, was likewise similar, starting from different values and increased with temperature, reaching 236 and 250 μV · K^{-1} at 1073 K for a CCO-30-35-10 nanocomposite ceramic perpendicular and parallel to the press-

ing direction, respectively. The absolute values of σ for the different materials increased with doping content of Tb. The simultaneous increases in σ and α indicate an increased charge carrier density n and carrier mobility μ in the nanocomposite ceramics. The impact of Bi on the thermoelectric properties of c-axis-oriented CCO thin films was reported by Sun et al. [46], and Saini et al. [38] showed that Tb-doping increased the value of μ.

3.3. Challenges in manufacturing

The manufacturing of a large, crack-free and homogeneous ceramic sample from uniaxially pressing and pressureless sintering in air, in order to measure the transport properties parallel to the pressing direction, is challenging. For this reason, thermoelectric properties parallel to the pressing direction were solely reported for the CCO-30-35-10 sample, which showed best values perpendicular to the pressing direction. In previous reports about the anisotropic properties of CCO, large and dense materials were obtained from cold isostatically pressing (CIP) [48], spark plasma sintering (SPS) [49] and hot-pressing (HP) [50, 51].

3.4. Figure-of-merit zT vs. Ioffe plot

The zT values of CCO and CCO-30-35-10 nanocomposite, shown in Figure 6d, were determined according to Equation 3, from the calculated power factor and the corresponding values of the heat conductivity λ perpendicular and parallel to the pressing direction, respectively. The λ values of the CCO-30-35-10 nanocomposite, as shown in Figure 6c, reached 1.96 and 1.1 $W \cdot m^{-1} \cdot K^{-1}$, respectively, at 1073 K perpendicular and parallel to the pressing direction. The anisotropy in the thermal transport properties is illustrated by the difference of the heat conductivity perpendicular and parallel to the pressing direction. Figure S 9[†] illustrates the measured values of the heat capacity C_P as a function of temperature in the range from 313 K to 1173 K. The heat capacity C_P reached approximately 0.83 $J \cdot K^{-1} \cdot g^{-1}$ at 1073 K for a CCO-30-35-10 nanocomposite. The trend and values of C_P as a function of temperature were similar to the values for pure CCO reported by Jankovsky et al. [52] and were consistent with phononic Debye-Einstein behavior. Values of the figure-of-merit zT at 1073 K, as shown in Figure 6d, were as follows: 0.4 (parallel to the pressing direction, CCO), 0.35 (perpendicular, CCO-30-35-10) and 0.31 (parallel, CCO-30-35-10). A very low heat conductivity λ, which is given in Figure 6c, led to a high zT value of CCO in the direction parallel to the pressing direction. However, CCO shows low values in the Ioffe plot of Figure 6b of both thermoelectric power factor $\sigma \cdot \alpha^2$ and electrical conductivity σ [33], which is detrimental for power generation.
The thermoelectric power factor of nanocomposites, calculated from σ and α perpendicular and parallel to the pressing direction, is shown in a Ioffe plot in Figure 6b as a function of the electrical conductivity. The Ioffe plot is suitable to estimate the capability of a thermoelectric material in power generation applications, due to the combined presentation of electrical conductivity σ and the power factor $\sigma \cdot \alpha^2$ [47]. A large improvement was observed due to the simultaneous enhancement of σ and α by Na, Bi and Tb co-doping and the formation of a nanocomposite material, which is, according to Equation 4, beneficial for power generation. The thermoelectric power factor of the CCO-30-35-10 nanocomposite, represented in Figure 6b, reached 6.5 and 3.2 $\mu W \cdot cm^{-1} \cdot K^{-2}$ at 1073 K, perpendicular and parallel to the pressing direction, respectively. The consideration of all parameters within the figure-of-merit zT, according to Equation 3, conceals the specific properties of the materials, a thermal isolator with low electrical conductivity can provide a high zT value. However, a thermal isolator, which has a high figure-of-merit zT, but poor electrical properties, is not useful for high electrical power generation. The Ioffe plot, illustrated in Figure 6b, which considers the thermoelectric power factor and the electrical conductivity, is more appropriate according to Equation 4, to evaluate the applicability of a material for high-temperature power generation.

3.5. Comparison and evaluation

Nanocomposites from pressureless sintering in air exhibited similar trends of the heat conductivity λ, but absolute values of 1.83, 1.79 and 1.96 $W \cdot m^{-1} \cdot K^{-1}$ at 1073 K differed, as shown in Figure 6c. Solely based on this Figure, the inclusions of NCO and BCCO appear to enhance the thermal conductivity. However, dense CCO materials from SPS [49] and HP [50] showed much higher λ values of 3.0 and 2.8 $W \cdot m^{-1} \cdot K^{-1}$ perpendicular to the pressing direction than dense nanocomposites presumably would. As a result, different microstructures, values of density and electrical conductivity of the pure CCO and CCO-NCO-BCCO nanocomposite ceramics make a comparison difficult. As shown in Figure 6c, the nanocomposite revealed a λ value of 1.1 $W \cdot m^{-1} \cdot K^{-1}$ at 1073 K parallel to the pressing direction. Previous reports about anisotropic transport properties in highly oriented CCO revealed a heat conductivity of 1.5 and 1.2 $W \cdot m^{-1} \cdot K^{-1}$ parallel to the pressing direction [49, 50]. Concerning the electrical conductivity σ and the Seebeck coefficient α, Nong et al. were able to enhance σ to about 130 $S \cdot cm^{-1}$ and α to approximately 235 $\mu V \cdot K^{-1}$ at 1073 K perpendicular

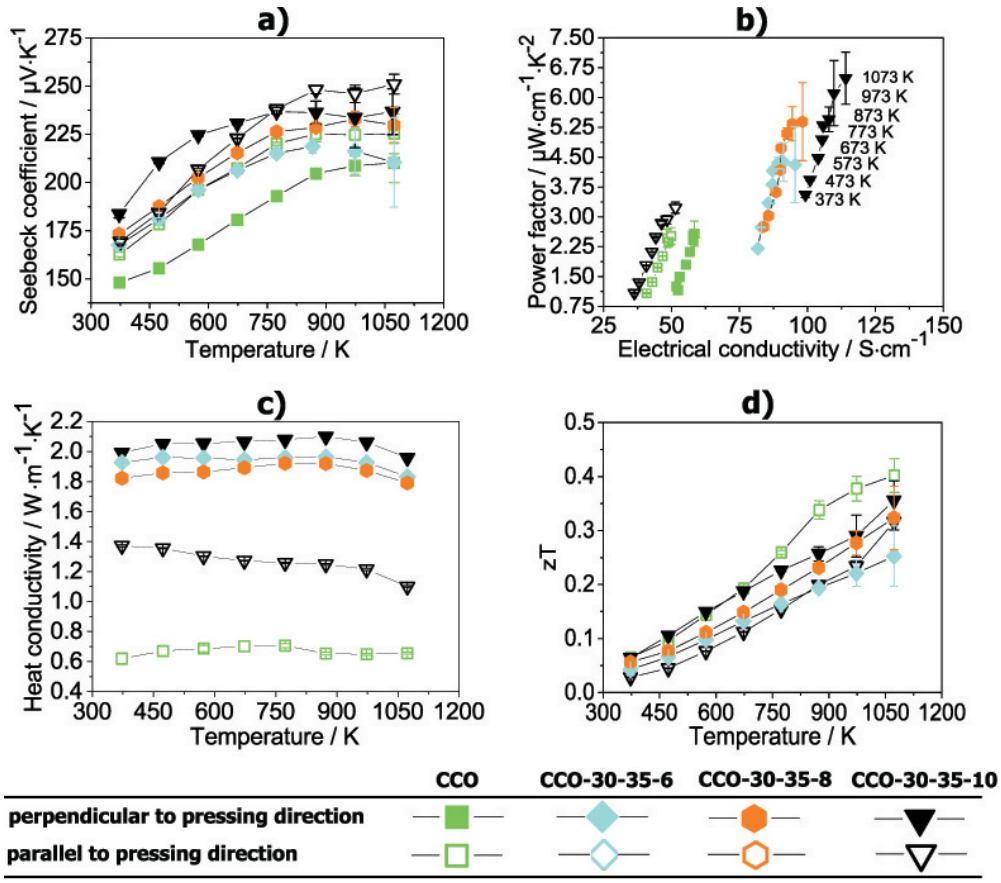

Figure 6: Thermoelectric parameters of **CCO** (square, green, taken from [33]), **CCO-30-35-6** (diamond, turquoise), **CCO-30-35-8** (hexagon, orange) and **CCO-30-35-10** (reverse rectangle, black) as a function of temperature: a) Seebeck coefficient α, b) Ioffe plot, power factor $\sigma \cdot \alpha^2$ as a function of σ [47], c) heat conductivity λ and d) figure-of-merit zT. Closed and open symbols represent values measured from samples perpendicular and parallel to the pressing direction, respectively. Uncertainties are indicated by error bars.

to the pressing direction by co-doping with Ag, Lu and spark plasma sintering of a dense material [26]. Saini et al. showed a significant increase in α by Tb-doping up to 325 $\mu V \cdot K^{-1}$ at 800 K for a $Ca_{3-x}Tb_xCo_4O_9$, x= 0.5 ceramic, perpendicular to the pressing direction [38]. By comparing the thermoelectric properties of the stacked 2D nanocomposite with the aforementioned reports, further improvements could be achieved with enhanced density, for example by utilization of alternative processing techniques. However, the comparison of the anisotropic thermoelectric properties of manufactured nanocomposites with CCO-based materials from literature is difficult. According to the used synthesis route and processing technique, the obtained properties like density, microstructure and degree of orientation of the materials are different. As a consequence, the obtained thermoelectric properties of these materials can not be easily compared to each other.

The pure phases of CCO [49], NCO [53] and BCCO [41] show a thermoelectric power factor of about 5, 3 and 1 $\mu W \cdot cm^{-1} \cdot K^{-2}$ at 1073 K, 900 K and 1000 K, respectively. These lower values of the thermoelectric power factors, compared to the triple-phase CCO-NCO-BCCO nanocomposite, were obtained from much higher polycrystalline bulk densities of 96-99 %. Strong anisotropy was also observed for σ and α, however, the values perpendicular and parallel to the pressing direction were enhanced due to co-doping and composite formation. The highest power factor and zT value were obtained perpendicular to the pressing direction for the CCO-30-35-10 nanocomposite. The high thermoelectric power factor $\sigma \cdot \alpha^2$, electrical conductivity σ, shown in the Ioffe plot in Figure 6b, and the moderate heat conductivity λ are beneficial for

power generation at high temperatures from infinite heat sources [31]. Thermoelectric materials should be designed and utilized in consideration of their application area, for example high energy conversion efficiency or high power generation. In this work, a high power material of semi-coherent 2D nanostructures was developed. This triple-phase nanocomposite has simultaneously enhanced thermoelectric properties and is applicable in the high-temperature range in air for thermoelectric power generation.

4. Conclusions

A material design of semi-coherently layered 2D nanostructures appears promising. Co-doping with suitable dopants can enhance the thermoelectric properties, but a triple-phase nanocomposite of co-doped phases provides synergistic effects and increases the thermoelectric properties. The formation of semi-coherent 2D nanostructures enabled the simultaneous enhancement of the thermoelectric properties σ and α. The BCCO and NCO phases are stabilized at elevated temperatures within a co-doped CCO-NCO-BCCO nanocomposite and beneficial properties were extended to the high-temperature range. The integration of materials that are unstable at high temperatures into a stable matrix could utilize synergistic effects and presents new alternatives in material development. The high electrical conductivity and power factor, revealed by the Ioffe plot, offer the application in a thermoelectric generator for waste heat recovery at high temperatures in air. The evaluation of thermoelectric materials for power generation at high temperatures should be discussed critically, since the figure-of-merit zT is misleading to determine the applicability. The Ioffe plot, which shows the thermoelectric power factor as a function of the electrical conductivity, is more suitable to evaluate the ability for high-temperature power generation.

5. Acknowledgment

This work has been funded by the Deutsche Forschungsgesellschaft (DFG, German Research Foundation) - FE928/17-1. Financial support from The Research Council of Norway is appreciated under the program Nano2021 to the project (Number 228854) "Thermoelectric materials: Nanostructuring for improving the energy efficiency of thermoelectric generators and heat-pumps" (THELMA). Thanks are to the E.ON Stipendienfonds (T0087 - ESF) for financing the academic exchange between the Norwegian University for Science and Technology (NTNU) and the Gottfried Wilhelm Leibniz University Hannover.

6. References

[1] H. U. Fuchs, A direct entropic approach to uniform and spatially continuous dynamical models of thermoelectric devices, EHS 1(3-4) (2014) 253–265.
[2] A. Feldhoff, Thermoelectric material tensor derived from the Onsager - de Groot - Callen model, EHS 2 (1) (2015) 5–13.
[3] A. F. Ioffe, Physics of Semiconductors, 1st Edition, Infosearch Ltd. London, 1960.
[4] Y. Miyazaki, M. Onoda, T. Oku, M. Kikuchi, Y. Ishii, Y. Ono, Y. Morii, T. Kajitani, Modulated structure of thermoelectric compound $[Ca_2CoO_3]$ CoO_2, J. Phys. Soc. Jpn. 71 (2002) 491–497.
[5] H. Muguerra, D. Grebille, E. Guilmeau, R. Cloots, Modulated misfit structure of the thermoelectric $[Bi_{0.84}CoO_2][CoO_2]_{1.69}$ cobalt oxide, Inorg. Chem. 47 (2008) 2464–2471.
[6] L. Viciu, J. W. G. Bos, H. W. Zandbergen, Q. Huang, M. L. Foo, S. Ishiwata, A. P. Ramirez, M. Lee, N. P. Ong, R. J. Cava, Crystal structure and elementary properties of Na_xCoO_2 (x = 0.32, 0.51, 0.6, 0.75, and 0.92) in the three-layer $NaCoO_2$ family, Phys. Rev. B 73 (2006) 174104–1–174104–10.
[7] M. G. Kanatzidis, Nanostructured thermoelectrics: The new paradigm?, Chem. Mater. 22 (2010) 648–659.
[8] M. Martín-González, O. Caballero-Calero, P. Díaz-Chao, Nanoengineering thermoelectrics for 21st century: Energy harvesting and other trends in the field, Renew. Sust. Energ. Rev. 24 (2013) 288–305.
[9] J. Yang, H.-L. Yip, A. K.-Y. Jen, Rational design of advanced thermoelectric materials, Adv. Energy Mater. 3 (2013) 549.
[10] G. Tan, L.-D. Zhao, M. Kanatzidis, Rationally designing high-performance bulk thermoelectric materials, Chem. Rev. 116 (2016) 12123–12149.
[11] M. S. Dresselhaus, G. Chen, M. Y. Tang, R. Yang, H. Lee, D. Wang, Z. Ren, J. P. Fleurial, P. Gogna, New directions for low-dimensional thermoelectric materials, Adv. Mater. 19 (2007) 1043–1053.
[12] D. L. Medlin, G. J. Snyder, Interfaces in bulk thermoelectric materials a review for current opinion in colloid and interface science, Curr. Opin. Colloid In. 14 (2009) 226–235.
[13] J. P. Heremans, B. Wiendlocha, A. M. Chamoire, Resonant levels in bulk thermoelectric semiconductors, Energ. Environ. Sci. 5 (2012) 5510–5530.
[14] Y. Pei, X. Shi, A. Lalonde, H. Wang, L. Chen, G. J. Snyder, Convergence of electronic bands for high performance bulk thermoelectrics, Nature 473 (2011) 66–69.
[15] R. J. Korkosz, T. C. Chasapis, S.-H. Lo, J. W. Doak, Y. J. Kim, C.-I. Wu, E. Hatzikraniotis, T. P. Hogan, D. N. Seidman, D. Wolverton, V. P. Dravid, M. G. Kanatzidis, High ZT in p-type $(PbTe)_{1-2x}(PbSe)_x(PbS)_x$ thermoelectric materials, J. Am. Chem. Soc. 136 (2014) 3225–3237.
[16] D. Wu, L.-D. Zhao, X. Tong, W. Li, L. Wu, Q. Tan, Y. Pei, L. Huang, J.-F. Li, Y. Zhu, M. G. Kanatzidis, J. He, Superior thermoelectric performance in PbTe-PbS pseudo-binary: extremely low thermal conductivity and modulated carrier concentration, Energ. Environ. Sci. 8 (2015) 2056–2068.
[17] C. Fu, T. Zhu, Y. Liu, H. Xie, X. Zhao, Band engineering of high performance p-type FeNbSb based half-Heusler thermoelectric materials for figure of merit zT > 1, Energ. Environ. Sci. 8 (2015) 216–220.
[18] J. P. Heremans, V. Jovovic, E. S. Toberer, A. Saramat, K. Kurosaki, A. Charoenphakdee, S. Yamanaka, G. J. Snyder,

Enhancement of thermoelectric efficiency in PbTe by distortion of the electronic density of states, Science 321 (2008) 554–557.
[19] L. D. Hicks, M. S. Dresselhaus, Thermoelectric figure of merit of a one-dimensional conductor, Phys. Rev. B 47 (1993) 16631–16634.
[20] G. J. Snyder, E. S. Toberer, Complex thermoelectric materials, Nat. Mater. 7 (2008) 105–114.
[21] G. Joshi, H. Lee, Y. Lan, X. Wang, G. Zhu, D. Wang, R. Gould, D. C. Cuff, M. Y. Tang, M. S. Dresselhaus, G. Chen, Z. Ren, Enhanced thermoelectric figure-of-merit in nanostructured p-type silicon germanium bulk alloys, Nano. Lett. 8 (2008) 4670–4674.
[22] L.-D. Zhao, S.-H. Lo, Y. Zhang, H. Sun, G. Tan, C. Uher, C. Wolverton, V. P. Dravid, M. G. Kanatzidis, Ultralow thermal conductivity and high thermoelectric figure of merit in SnSe crystals, Nature 508 (2014) 373–377.
[23] S. R. Brown, S. M. Kauzlarich, F. Gascoin, G. J. Snyder, $Yb_{14}MnSb_{11}$: New high efficiency thermoelectric material for power generation, Chem. Mater. 18 (2006) 1873–1877.
[24] D. M. Rowe, CRC Handbook of Thermoelectrics, 89th Edition, CRC Press, Boca Raton, FL, 1995.
[25] M. Ohtaki, K. Araki, K. Yamamoto, High thermoelectric performance of dually doped ZnO ceramics, J. Electron. Mater. 38 (2009) 1234–1238.
[26] N. V. Nong, N. Pryds, S. Linderoth, M. Ohtaki, Enhancement of the thermoelectric performance of p-type layered oxide $Ca_3Co_4O_{9+\delta}$ through heavy doping and metallic nanoinclusions, Adv. Mater. 23 (2011) 2484–2490.
[27] J. Sui, J. Li, J. He, Y.-L. Pei, D. Berardan, H. Wu, N. Dragoe, W. Cai, L.-D. Zhao, Texturation boosts the thermoelectric performance of BiCuSeO oxyselenides, Energ. Environ. Sci. 6 (2013) 2916–2920.
[28] Y. Liu, L.-D. Zhao, Y. Zhu, Y. Liu, F. Li, M. Yu, D.-B. Liu, W. Xu, Y.-H. Lin, C.-W. Nan, Synergistically optimizing electrical and thermal transport properties of BiCuSeO via a dual-doping approach, Adv. Energy Mater. 6 (2016) 1502423.
[29] G.-K. Ren, S.-Y. Wang, Y.-C. Zhu, K. J. Ventura, X. Tan, W. Xu, Y.-H. Lin, J. Yang, C.-W. Nan, Enhancing thermoelectric performance in hierarchically structured BiCuSeO by increasing bond covalency and weakening carrier-phonon coupling, Adv. Energy Mater. 10 (2017) 1590–1599.
[30] C. Barreteau, D. Berardan, N. Dragoe, Studies on the thermal stability of BiCuSeO, J. Solid State Chem. 222 (2015) 53–59.
[31] D. Narducci, Wo we really need high thermoelectric figure of merit? A critical appraisal to the power conversion efficiency of thermoelectric materials, Appl. Phys. Lett. 99 (2011) 102104–1–102104–3.
[32] Y. Miyazaki, Crystal structure and thermoelectric properties of the misfit-layered cobalt oxides, Solid State Ionics 172 (2004) 463–467.
[33] M. Bittner, L. Helmich, F. Nietschke, B. Geppert, O. Oeckler, A. Feldhoff, Porous $Ca_3Co_4O_9$ with enhanced thermoelectric properties derived from sol-gel synthesis, J. Eur. Ceram. Soc. 37 (2017) 3909–3915.
[34] N. Kanas, S. P. Singh, M. Rotan, M. Saleemi, M. Bittner, A. Feldhoff, T. Norby, K. Wiik, T. Grande, M.-A. Einarsrud, Influence of processing on stability, microstructure and thermoelectric properties of $Ca_3Co_{4-x}O_{9+\delta}$, J. Eur. Ceram. Soc. 38 (2018) 1592–1599.
[35] G. Xu, R. Funahashi, M. Shikano, I. Matsubara, Y. Zhou, Thermoelectric properties of the Bi- Na-substituted $Ca_3Co_4O_9$ system, Appl. Phys. Lett. 80 (2002) 3760–3762.
[36] Y. Masuda, D. Nagahama, H. Itahara, T. Tani, W. S. Seo, K. Koumoto, Thermoelectric performance of Bi- and Na-substituted $Ca_3Co_4O_9$ improved through ceramic texturing, J. Mater. Chem. 13 (2003) 1094–1099.
[37] A. I. Klyndyuk, I. V. Matsukevich, Synthesis and properties of $Ca_{2.8}Ln_{0.2}Co_4O_{9+\delta}$ (Ln = La, Nd, Sm, Tb-Er) solid solutions, Inorg. Mater+. 48 (2012) 1052–1057.
[38] S. Saini, H. S. Yaddanapudi, K. Tian, Y. Yin, D. Magginetti, A. Tiwari, Terbium ion doping in $Ca_3Co_4O_9$: A step towards high-performance thermoelectric materials, Sci. Rep-UK. 7 (2017) 44621.
[39] H. Leligny, D. Grebille, O. Pérez, A. C. Masset, M. Hervieu, B. Raveau, A five-dimensional structural investigation of the misfit layer compound $[Bi_{0.87}SrO_2]_2[CoO_2]_{1.82}$, Acta Cryst. B B56 (2000) 173–182.
[40] E. Guilmeau, M. Pollet, D. Grebille, M. Hervieu, M. Muguerra, R. Cloots, M. Mikami, R. Funahashi, Nanoblock coupling effect in iodine intercalated $[Bi_{0.82}CaO_2]_2[CoO_2]_{1.69}$ layered cobaltite, Inorg. Chem. 46 (2007) 2124–2131.
[41] A. Sotelo, E. Guilmeau, S. Rasekh, M. A. Madre, S. Marinel, J. C. Diez, Enhancement of the thermoelectric properties of directionally grown Bi-Ca-Co-O through Pb for Bi substitution, J. Eur. Ceram. Soc. 30 (2010) 1815–1820.
[42] I. V. Matsukevich, A. I. Klyndyuk, E. A. Tugova, A. N. Kovalenko, A. A. Marova, N. S. Krasutskaya, Thermoelectric properties of $Ca_{3-x}Bi_xCo_4O_{9+delta}$ ($0.0 \leq x \leq 1.5$) ceramics, Inorg. Mater+. 52 (2016) 644–650.
[43] A. Feldhoff, M. Arnold, J. Martynczuk, T. M. Gesing, H. Wang, The sol-gel synthesis of perovskites by EDTA/citrite complexing method involves nanoscale solid state reactions, Solid State Sci. 10 (2008) 689–701.
[44] T. Janssen, A. Janner, A. Looijenga-Vos, P. M. De Wolff, International Tables for Crystallography: 9.8 Incommensurate and commensurate modulated structures, Volume C Edition, Kluwer Academic Publishers, Dordrecht/Boston/London, 2004.
[45] M. Lee, L. Viciu, Y. Wang, M. L. Foo, S. Watauchi, R. A. Pascal JR, R. J. Cava, N. P. Ong, Large enhancement of the thermopower in Na_xCoO_2 at high Na doping, Nat. Mater. 5 (2006) 537–540.
[46] T. Sun, H. H. Hng, Q. Y. Yan, J. Ma, Enhanced high temperature thermoelectric properties of Bi-doped c-axis oriented $Ca_3Co_4O_9$ thin films by pulsed laser deposition, J. Appl. Phys. 108(8) (2010) 3709.
[47] Q. Zhu, E. M. Hopper, B. J. Ingram, T. O. Mason, Combined Jonker and Ioffe analysis of oxide conductors and semiconductors, J. Am. Ceram. Soc. 94 (2011) 187–193.
[48] J.-W. Moon, D. Nagahama, Y. Masuda, W.-S. Seo, K. Koumoto, Anisotropic thermoelectric properties of crystal-axis oriented ceramics of layer-structured oxide in the Ca-Co-O system, J. Ceram. Soc. Jpn. 109 (2001) 647–650.
[49] C.-H. Lim, H.-H. Park, S.-M. Choi, K.-H. Lee, K. Park, Anisotropy of the thermoelectric figure of merit (ZT) in textured $Ca_3Co_4O_9$ ceramics prepared by using a spark plasma sintering process, J. Korean. Phys. Soc. 66 (2015) 794–799.
[50] D. Kenfaui, B. Lenoir, D. Chateigner, B. Ouladdiaf, M. Gomina, J. G. Noudem, Development of multilayer textured $Ca_3Co_4O_9$ materials for thermoelectric generators: Influence of the anisotropy on the transport properties, J. Eur. Ceram. Soc. 32 (2012) 2405–2414.
[51] D. Kenfaui, D. Chateigner, M. Gomina, J. G. Noudem, B. Ouladdiaf, A. Dauschner, B. Lenoir, Volume texture and anisotropic thermoelectric properties in $Ca_3Co_4O_9$ bulk materials, Mater. Today. 2 (2015) 637–646.
[52] O. Jankovsky, D. Sedmidubsky, Z. Sofer, J. Hejtmanek, Thermodynamic behavior of $Ca_3Co_4O_{9+\delta}$ ceramics, Ceram-Silikaty 56(2) (2012) 139–144.
[53] J.-Y. Tak, K. H. Lee, J.-Y. Kim, C.-H. Lim, W.-S. Seo, Y. S. Lim, H. K. Cho, S.-M. Choi, Optimization of synthesis conditions of $Na_{0.75}CoO_2$ for high thermoelectric performance, J. Electron.

Mater. 44 (2014) 1408–1412.